

Computational Biology

Bir Bhanu  
Prue Talbot *Editors*

# Video Bioinformatics

From Live Imaging to Knowledge



**EXTRAS ONLINE**

 Springer

# Computational Biology

## Volume 22

### Editors-in-Chief

Andreas Dress

CAS-MPG Partner Institute for Computational Biology, Shanghai, China

Michal Linial

Hebrew University of Jerusalem, Jerusalem, Israel

Olga Troyanskaya

Princeton University, Princeton, NJ, USA

Martin Vingron

Max Planck Institute for Molecular Genetics, Berlin, Germany

### Editorial Board

Robert Giegerich, University of Bielefeld, Bielefeld, Germany

Janet Kelso, Max Planck Institute for Evolutionary Anthropology, Leipzig, Germany

Gene Myers, Max Planck Institute of Molecular Cell Biology and Genetics, Dresden, Germany

Pavel A. Pevzner, University of California, San Diego, CA, USA

### Advisory Board

Gordon Crippen, University of Michigan, Ann Arbor, MI, USA

Joe Felsenstein, University of Washington, Seattle, WA, USA

Dan Gusfield, University of California, Davis, CA, USA

Sorin Istrail, Brown University, Providence, RI, USA

Thomas Lengauer, Max Planck Institute for Computer Science, Saarbrücken, Germany

Marcella McClure, Montana State University, Bozeman, MO, USA

Martin Nowak, Harvard University, Cambridge, MA, USA

David Sankoff, University of Ottawa, Ottawa, ON, Canada

Ron Shamir, Tel Aviv University, Tel Aviv, Israel

Mike Steel, University of Canterbury, Christchurch, New Zealand

Gary Stormo, Washington University in St. Louis, St. Louis, MO, USA

Simon Tavaré, University of Cambridge, Cambridge, UK

Tandy Warnow, University of Texas, Austin, TX, USA

Lonnie Welch, Ohio University, Athens, OH, USA

The *Computational Biology* series publishes the very latest, high-quality research devoted to specific issues in computer-assisted analysis of biological data. The main emphasis is on current scientific developments and innovative techniques in computational biology (bioinformatics), bringing to light methods from mathematics, statistics and computer science that directly address biological problems currently under investigation.

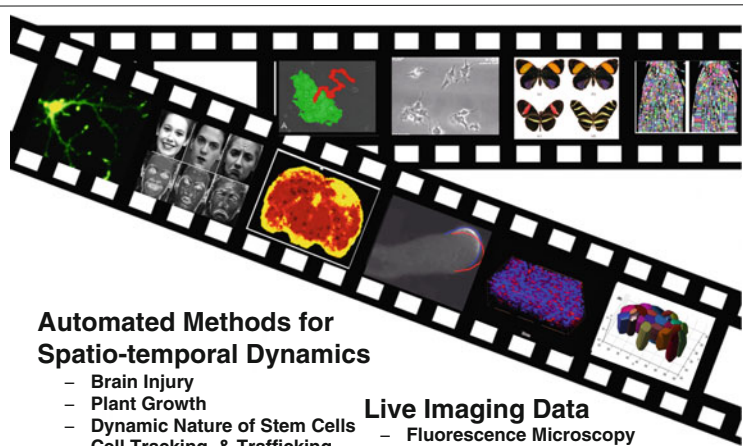
The series offers publications that present the state-of-the-art regarding the problems in question; show computational biology/bioinformatics methods at work; and finally discuss anticipated demands regarding developments in future methodology. Titles can range from focused monographs, to undergraduate and graduate textbooks, and professional text/reference works.

More information about this series at <http://www.springer.com/series/5769>

Bir Bhanu · Prue Talbot  
Editors

# Video Bioinformatics

From Live Imaging to Knowledge



**Automated Methods for  
Spatio-temporal Dynamics**

- Brain Injury
- Plant Growth
- Dynamic Nature of Stem Cells
- Cell Tracking & Trafficking
- Changing Morphology
- Facial Expressions

**Live Imaging Data**

- Fluorescence Microscopy
- Phase Contrast Imaging
- Optical Coherence Tomography
- Magnetic Resonance Imaging
- Brightfield Imaging

*Editors*

Bir Bhanu  
University of California  
Riverside, CA  
USA

Prue Talbot  
University of California  
Riverside, CA  
USA

ISSN 1568-2684

Computational Biology

ISBN 978-3-319-23723-7

ISBN 978-3-319-23724-4 (eBook)

DOI 10.1007/978-3-319-23724-4

Library of Congress Control Number: 2015950871

Springer Cham Heidelberg New York Dordrecht London

© Springer International Publishing Switzerland 2015

© Springer International Publishing Switzerland (outside the USA) 2015 for Chapter 9

This work is subject to copyright. All rights are reserved by the Publisher, whether the whole or part of the material is concerned, specifically the rights of translation, reprinting, reuse of illustrations, recitation, broadcasting, reproduction on microfilms or in any other physical way, and transmission or information storage and retrieval, electronic adaptation, computer software, or by similar or dissimilar methodology now known or hereafter developed.

The use of general descriptive names, registered names, trademarks, service marks, etc. in this publication does not imply, even in the absence of a specific statement, that such names are exempt from the relevant protective laws and regulations and therefore free for general use.

The publisher, the authors and the editors are safe to assume that the advice and information in this book are believed to be true and accurate at the date of publication. Neither the publisher nor the authors or the editors give a warranty, express or implied, with respect to the material contained herein or for any errors or omissions that may have been made.

Printed on acid-free paper

Springer International Publishing AG Switzerland is part of Springer Science+Business Media  
([www.springer.com](http://www.springer.com))

# Preface

The recent advances in high-throughput technologies for functional genomics and proteomics have revolutionized our understanding of living processes. However, these technologies, for the most part, are limited to a *snapshot analysis* of biological processes that are by nature *continuous and dynamic*. Modern visual microscopy enables video imaging of cellular and molecular dynamic events and provides unprecedented opportunities to understand how spatiotemporal dynamic processes work in a cellular and multicellular system. The application of these technologies is becoming a mainstay of the biological sciences worldwide. To gain a more mechanistic and systematic understanding of biological processes, we need to elucidate cellular and molecular dynamic processes and events.

**Video Bioinformatics** as defined by the first author (BB) is concerned with the automated processing, analysis, understanding, data mining, visualization, query-based retrieval/storage of biological spatiotemporal events/data and knowledge extracted from microscopic videos. It integrates expertise from the life sciences, computer science and engineering to enable breakthrough capabilities in understanding continuous biological processes. The video bioinformatics information related to spatiotemporal dynamics of specific molecules/cells and their interactions in conjunction with genome sequences are essential to understand how genomes create cells, how cells constitute organisms, and how errant cells cause disease.

Currently, new imaging instrumentation and devices perform *live video imaging* to image molecules and subcellular structures in living cells and collect biological videos for on-line/off-line processing. We can now see and study the complex molecular machinery responsible for the formation of new cells. Multiple imaging modalities can provide 2D to 5D (3D space, time, frequency/wavelength) data since we can image 2D/3D objects for seconds to months and at many different wavelengths. However, data processing and analysis (informatics) techniques for handling biological images/videos have lagged significantly and they are at their infancy. There are several reasons for this, such as the complexity of biological videos which are more challenging than the structured medical data, and the lack of

interdisciplinary research at the intersection of life sciences and engineering and computer science.

We already are at a point where researchers are overwhelmed by myriads of high-quality videos without proper tools for their organization, analysis, and interpretation. This is the main reason why video data are currently underutilized. We believe that the next major advance in imaging of biological samples will come from advances in the automated analysis of multi-dimensional images. Having tools that enable processes to be studied rapidly and conveniently over time will, like Hooke's light microscope and Ruska's electron microscope, open up a new world of analysis to biologists, scientists, and engineers.

This interdisciplinary book on *Video Bioinformatics* presents computational techniques for the solution of biological problems of significant current interest such as 2D/3D live imaging, mild-traumatic brain injury, human embryonic stem cells, growth of pollen tubes, cell tracking, cell trafficking, etc. The analytical approaches presented here will enable the study of biological processes in 5D in large video sequences and databases. These computational techniques will provide greater sensitivity, objectivity, and repeatability of biological experiments. This will make it possible for massive volumes of video data to be analyzed efficiently, and many of the fundamental questions in life sciences and informatics be answered. The book provides examples of these challenges for video understanding of cell dynamics by developing innovative techniques. Multiple imaging modalities at varying spatial and temporal resolutions are used in conjunction with computational methods for video mining and knowledge discovery.

The book deals with many of the aspects of the video bioinformatics as defined above. Most of the chapters that follow represent the work that was completed as part of an NSF-funded IGERT program in Video Bioinformatics at the University of California in Riverside. Several of the chapters deal with work that keynote speakers presented at retreats sponsored by this program (Chaps. 14 and 16). Most other chapters are work done by IGERT Ph.D. fellows who were selected to participate in this program. The program emphasizes an interdisciplinary approach to data analysis with graduate students from engineering and life sciences being paired to work together as teams. These resulting chapters would likely never have been produced without cooperation between these two distinct disciplines and demonstrate the power of this type in interdisciplinary cooperation.

We appreciate the suggestions, support feedback and encouragement received from the IGERT faculty, IGERT fellows and NSF IGERT Program Directors Richard Tankersley, M.K. Ramasubramanian, Vikram Jaswal, Holly K. Given, and Carol Stoel. Authors would like to thank Dean Reza Abbaschian, Dean Joe Childers, Dallas Rabenstein, David Eastman, Victor Rodgers, Zhenbiao Yang, Vassilis Tsotras, Dimitri Morikis, Aaron Seitz, Jiayu Liao, David Carter, Jerry Schultz, Lisa Kohne, Bill Bingham, Mitch Boretz, Jhon Gonzalez, Michael Caputo, Michael Dang and Benjamin Davis for their support and help with the IGERT program. Authors would also like to thank Atena Zahedi for the sketch shown on the inside title page. Further, the authors would like to thank Simon Rees and Wayne Wheeler of Springer and Priyadarshini Senthilkumar (Scientific Publishing

Services) for their efforts related with the publication of this book. The first author (BB) would like to acknowledge the support from National Science Foundation grants DGE 0903667 video bioinformatics, CNS 1330110 distributed sensing, learning and control, IIS 0905671 video data mining, IIS 0915270 performance prediction, CCF 0727129 bio-inspired computation, and DBI 0641076 morphological databases. The second author (PT) would like to acknowledge support from the Tobacco Related Disease Research Program of California (18XT-0167; 19XT-0151; 20XT-0118; 22RT-0217), the California Institute of Regenerative Medicine (CL1-00508), and NIH (R01 DA036493; R21 DA037365).

Riverside, CA, USA  
June 2015

Bir Bhanu  
Prue Talbot



# List of Video Links with QR Codes

## Software for Using QR Codes:

In order to scan a QR Code you must install a QR Code reader app on your smartphone. You can download an app on Google Play (Android Market), Blackberry AppWorld, App Store (iOS/iPhone), or Windows Phone Marketplace.

- Most QR scanning apps are free. Any app that can read barcodes should be able to process QR codes.
- Recommended for Android: Google Goggles Version 1.9.4
- Recommended for iOS: Quick Scan—QR Code Reader Version 1.1.5

## Hyperlinks and QR Codes for each Video Referenced in the Book

IGERT on Video Bioinformatics YouTube Channel:

<https://www.youtube.com/channel/UCX9tYZRm-mGwhg6866FWizA>

Chapter 6:

Video 1: <https://www.youtube.com/watch?v=3ylu3oHZEC4>



Video 2: <https://www.youtube.com/watch?v=sfNhuK9JSxA>



Chapter 8:

Video 1: <https://www.youtube.com/watch?v=dQTkldB8lNk>



Video 2: <https://www.youtube.com/watch?v=NgJZ49xgev8>



Video 3: [https://www.youtube.com/watch?v=plb\\_CInFoEY](https://www.youtube.com/watch?v=plb_CInFoEY)



Video 4: <https://www.youtube.com/watch?v=tHJ5JDcpkWY>



Chapter 9:

Video 1: [https://www.youtube.com/watch?v=wN1F\\_K\\_2vsg](https://www.youtube.com/watch?v=wN1F_K_2vsg)



Video 2: <https://www.youtube.com/watch?v=INrVYlemvCY>



Video 3: <https://www.youtube.com/watch?v=xUcU3HpiMwI>



Video 4: <https://www.youtube.com/watch?v=RAiqZtK80Dw>



Video 5: <https://www.youtube.com/watch?v=hYayvIvuzOM>



Video 6: <https://www.youtube.com/watch?v=KLaFIhkovPI>



Video 7: [https://www.youtube.com/watch?v=Orw\\_IUs8KFI](https://www.youtube.com/watch?v=Orw_IUs8KFI)



Video 8: <https://www.youtube.com/watch?v=M-asAiwLnM>



Video 9: <https://www.youtube.com/watch?v=OHD0j74qbk0>



Video 10: <https://www.youtube.com/watch?v=aZlbfqfDDyg>



Video 11: <https://www.youtube.com/watch?v=OTBt1WBqqGw>



Chapter 11:

Video 1: <https://www.youtube.com/watch?v=l-Sb2iqzw1Y>



Chapter 12:

Video 1: <https://www.youtube.com/watch?v=jvdL7L4nQIs>



Chapter 15:

Video 1: <https://www.youtube.com/watch?v=pxg14SdvNBc>



Video 2: <https://www.youtube.com/watch?v=NnPHrGxJ7j0>



Chapter 18:

Video 1: [https://www.youtube.com/watch?v=6KZc6e\\_EuGg](https://www.youtube.com/watch?v=6KZc6e_EuGg)



# Contents

## Part I Video Bioinformatics: An Introduction

- 1 **Live Imaging and Video Bioinformatics** . . . . . 3  
Bir Bhanu and Prue Talbot
- 2 **Video Bioinformatics Methods for Analyzing Cell Dynamics:  
A Survey** . . . . . 13  
Nirmalya Ghosh

## Part II Organismal Dynamics: Analyzing Brain Injury and Disease

- 3 **High- and Low-Level Contextual Modeling for the Detection  
of Mild Traumatic Brain Injury** . . . . . 59  
Anthony Bianchi, Bir Bhanu and Andre Obenaus
- 4 **Automated Identification of Injury Dynamics After Neonatal  
Hypoxia-Ischemia** . . . . . 77  
Nirmalya Ghosh, Stephen Ashwal and Andre Obenaus
- 5 **A Real-Time Analysis of Traumatic Brain Injury from  
T2 Weighted Magnetic Resonance Images  
Using a Symmetry-Based Algorithm** . . . . . 99  
Ehsan T. Esfahani, Devin W. McBride, Somayeh B. Shafiei  
and Andre Obenaus
- 6 **Visualizing Cortical Tissue Optical Changes During Seizure  
Activity with Optical Coherence Tomography** . . . . . 119  
M.M. Eberle, C.L. Rodriguez, J.I. Szu, Y. Wang, M.S. Hsu,  
D.K. Binder and B.H. Park

### Part III Dynamics of Stem Cells

- 7 Bio-Inspired Segmentation and Detection Methods for Human Embryonic Stem Cells** . . . . . 135  
Benjamin X. Guan, Bir Bhanu, Prue Talbot and Jo-Hao Weng
- 8 A Video Bioinformatics Method to Quantify Cell Spreading and Its Application to Cells Treated with Rho-Associated Protein Kinase and Blebbistatin** . . . . . 151  
Nikki Jo-Hao Weng, Rattapol Phandthong and Prue Talbot
- 9 Evaluation of Dynamic Cell Processes and Behavior Using Video Bioinformatics Tools** . . . . . 167  
Sabrina C. Lin, Henry Yip, Rattapol Phandthong, Barbara Davis and Prue Talbot

### Part IV Dynamic Processes in Plant and Fungal Systems

- 10 Video Bioinformatics: A New Dimension in Quantifying Plant Cell Dynamics** . . . . . 189  
Nolan Ung and Natasha V. Raikhel
- 11 Understanding Growth of Pollen Tube in Video** . . . . . 201  
Asongu L. Tambo, Bir Bhanu, Nan Luo and Zhenbiao Yang
- 12 Automatic Image Analysis Pipeline for Studying Growth in Arabidopsis** . . . . . 215  
Katya Mkrtychyan, Anirban Chakraborty, Min Liu and Amit Roy-Chowdhury
- 13 Quantitative Analyses Using Video Bioinformatics and Image Analysis Tools During Growth and Development in the Multicellular Fungus *Neurospora crassa*** . . . . . 237  
Ilva E. Cabrera, Asongu L. Tambo, Alberto C. Cruz, Benjamin X. Guan, Bir Bhanu and Katherine A. Borkovich

### Part V Dynamics of Intracellular Molecules

- 14 Quantification of the Dynamics of DNA Repair to Ionizing Radiation via Colocalization of 53BP1 and  $\gamma$ H2AX** . . . . . 253  
Torsten Groesser, Gerald V. Fontenay, Ju Han, Hang Chang, Janice Pluth and Bahram Parvin
- 15 A Method to Regulate Cofilin Transport Using Optogenetics and Live Video Analysis** . . . . . 265  
Atena Zahedi, Vincent On and Iryna Ethell

**Part VI Software, Systems and Databases**

**16 Integrated 5-D Cell Tracking and Linked Analytics in the FARSIGHT Open Source Toolkit . . . . . 283**  
Amine Merouane, Arunachalam Narayanaswamy and Badrinath Roysam

**17 Video Bioinformatics Databases and Software . . . . . 313**  
Ninad S. Thakoor, Alberto C. Cruz and Bir Bhanu

**18 Understanding of the Biological Process of Nonverbal Communication: Facial Emotion and Expression Recognition. . . . . 329**  
Alberto C. Cruz, B. Bhanu and N.S. Thakoor

**19 Identification and Retrieval of Moth Images Based on Wing Patterns . . . . . 349**  
Linan Feng, Bir Bhanu and John Heraty

**Index . . . . . 371**



# List of Figures

Figure 2.1	Conceptual diagram of a typical video bioinformatics system . . . . .	15
Figure 2.2	Interdependency of different low and midlevel image processing modules in bioinformatics . . . . .	17
Figure 2.3	Different types of extraction, recombination, and selection methods for static image features and interrelations between them. . . . .	23
Figure 2.4	Major pattern recognition techniques utilized in cellular and tissue classification in biological datasets . . . . .	34
Figure 2.5	Bioinformatics modules in large-scale biological dynamic databases that are often distributed across the globe and datamined by complex content-based queries over the Internet . . . . .	42
Figure 3.1	Graphical representation of the Bayesian network showing the dependencies of random variables. Intuitive definition of distributions: $A$ —anatomical constraints, $L_1, L_2$ —central location of injury for injury one and two, $H_1$ —time since the first event, $H_2$ —time between first and second injury, $Q$ —volume (quantity) of injury with time, $S_1, S_2$ —spread for first and second injury, $M$ —max operator, $V$ —visual information, $I$ —estimated injury. Where $I = 1$ is absolute certainty of injury and $I = 0$ is absolute certainty of NABM (normal appearing brain matter) . . . . .	62
Figure 3.2	A typical example of the fusion between visual and contextual models in a rat mTBI. In this example, the rat experienced two mTBIs several days apart to opposite brain hemispheres. <i>Top</i> Probability map after pSVM. <i>Middle</i> Probability map from the contextual model. <i>Bottom</i> Fusion of the contextual	

and visual models. Note that this illustrates that the contextual model for repeated injuries progress at different rates (compare hemispheres, where the right hemisphere was injured first) . . . . . 66

Figure 3.3 Experimental design. **a** Illustration of the mTBI locations for the first (*right*) and second (*left*) injuries. **b** Experimental mTBI and neuroimaging timeline. A single mTBI was induced to the *right* cortex on day 0 (denoted as an \*) in all animals. A second mTBI was induced to the left cortex at either 3 or 7 days later (\*). MR imaging was performed 1 day post-first (1d), 1 day post-last (4 day rmTBI 3 day, 8 day rmTBI 7 day) and 14 day post-injury (17 day rmTBI 3 day, 21 day rmTBI 7 day) (*red circles*) . . . . . 67

Figure 3.4 **a** ROC plot with multiple contextual inputs. Results were evaluated after thresholding the output probability map. **b** Dice plot with multiple contextual inputs. The peak of the Dice curve (maximum dice coefficient) is used to threshold the output probability map. Legends in (**b**) are the same as in (**a**) . . . . . 68

Figure 3.5 Example outputs from the thresholded probability maps (for single and repeated mTBI) with varying levels of contextual input. The thresholds were selected at the highest point on the dice curve for each respective level of context. Each row is a coronal slice, where the *top* is from a single mTBI and the *bottom* is from a repeated mTBI. The colors represent the following: *Green* true positive, *Teal* true negative, *Red* false positive, *Brown* false negative . . . . . 69

Figure 3.6 Overview of the proposed system where context information is sent from one classifier to the next at each time point. This information is then propagated to the next time point . . . . . 70

Figure 3.7 **a** Illustration of the proximity feature.  $V$  is the observed voxel and the feature is the average probability of the regions ( $R_1, R_2, R_3$ ). **b** Illustration of the distance features.  $V$  is the observed voxel and an example feature is the average probability between  $P_1$  and  $P_2$  along the  $45^\circ$  ray . . . . . 71

Figure 3.8 **a** Example MPM estimate. **b** Corresponding PMED feature. Note that the values become more negative toward the center of the object and more positive farther away from the object . . . . . 72

Figure 3.9 Dice coefficients after thresholding the posterior probability map at the end of each cascade of classifier (i.e., at each time point). This is the average of all the tests in the leave-one-out validation . . . . . 73

Figure 3.10 Qualitative results of the proposed approach using dynamic and static contextual features. Each coronal slice is from a separate volume. *Color code: yellow = true positive, black = true negative, orange = false negative, brown = false positive.* . . . . . 74

Figure 4.1 Comparative HII lesion dynamics results between HRS, SIRG and MWS computational methods. **a** The ischemic lesion detected (*red-border*) by manual and compared methods from representative serial T2 data are similar. **b** Lesion volumes at later time points are similar, but there are clear differences at the earlier imaging time points between computational methods. **c, d, and e** Overall computational performances for lesion location are compared for sensitivity, specificity, and similarity. HRS and SIRG performances were similar while MWS was not as accurate in all respects . . . . . 82

Figure 4.2 Long term lesion dynamics from serial T2 weighted MRI data: HRS detected lesion volumes closely matched with the ground-truth of manually derived results. Lesion volume initially decreases at 4–7 days post HII (see the initial sharp drop in injury volume) and then gradually increases and reaches its final size by 15–18 weeks. Note that, HRS includes ventricular hypertrophy (5–10 %) in late imaging time-points, which human observers typically ignore. . . . . 83

Figure 4.3 Spatiotemporal evolution of ischemic core-penumbra. **a** Temporal HRS detections of ischemic core (*red*) and penumbra (*blue*) from serial T2-weighted MRI at representative brain depth (from anterior-to-posterior scan) demonstrate evolving anatomical involvement over time. **b** HRS extracted volumetric lesion components identifies the proportional compositions of core-penumbra within the entire lesion over time post HII. Large proportion of salvageable penumbra is quickly converted into non-salvageable necrotic core by 7 days post HII . . . . . 85

Figure 4.4 Effect of hypothermia treatment in core-penumbra (CP) evolution. Hypothermia or normothermia

(control group) treatment was applied for 24 h immediately post HII and serial DWI data was acquired to evaluate efficacy of HT therapy. **a** HRS derived core-penumbra superimposed on DWI data at 0 and 24 h clearly demonstrate that HT restricted lesion expansion. Comparative HRS/DC result in **b** mild and **c** moderate injury show delayed injury progression in HT group with both severities until 72 h when volume of HII lesion (and ischemic core) rapidly increases and thus overall reducing potential salvageability . . . . . 88

Figure 4.5 Therapeutic effect of stem cells implanted in contralateral cortex 3 days post HII. **a** HRS derived ischemic core (*red*) and penumbra (*blue*) in serial T2-weighted MRI data demonstrate partial restriction of HII expansion as implanted NSC migrates from injection site (*downward yellow arrow*) to the tissues close to HII (*rightward yellow arrow*). **b** Volumetric summary of core-penumbra evolution suggests presence of penumbra even 7–17 days post HII (4–14 days post NSC implantation) . . . . . 90

Figure 4.6 Stem cell detection using Susceptibility weighted imaging (SWI). **a** SWI data at different brain levels (at a single imaging time-point) visualized Fe-labeled NSCs (hypointensity regions) implanted in contralateral ventricles and migrated to the lesion (*right*) site through cerebrospinal fluid. HRS could detect small NSC regions that, in future studies can be tracked in serial SWI data to monitor NSC activity. **b** Superimposed NSC locations derived by HRS from serial T2-data (in Figure 4.5) demonstrated a clear migration of NSC from injection site in contralateral cortex towards lesion location—even as early as 4d post implantation. . . . . 92

Figure 5.1 Representative T2-weighted MR images and pseudo-code for the automatic algorithm. **a** Representative Sham (surgery, no TBI) and a repetitive TBI. The MR images were obtained 1 day after the first (1st TBI) and the second (2nd TBI) injury. The injured hemisphere (*dotted line, sham*) is expanded to illustrate the manual ROI that were used to delineate the brain injury lesion. After the first TBI there was primarily edema present but after the 2nd TBI there appeared significant amounts of blood

(see also Figure 5.5). **b** Pseudo code for our automated algorithm that is composed of two primary components, skull stripping (see Figure 5.2) followed by lesion detection (see Figure 5.3) . . . . . 103

Figure 5.2 Primary skull stripping components. Level set initialization: **a** inputs for skull stripping included both T2-weighted MR images and the quantitative T2 map (T2 values, ms). **b** Foreground separations, **c** Morphological cleaning composed of cumulative roundness index (CRI) and delineation of the brain bounding box. **d** 2D results were validated using 3D connectivity testing. Level set algorithm: here the final brain area is found for each slice and then summed to identify the brain volume in 3D (see manuscript for additional details) . . . . . 107

Figure 5.3 Lesion detection components for naive, 1st TBI 1 day post injury, and 2nd TBI 3 days post injury examples. **a** Firstly, the algorithm identifies the axis of symmetry. **b** Seed point selections for edema and blood using asymmetry. **c** Region growing/shrinking based on the intensity of asymmetry for edema and blood. **d** Final lesion area(s) of brain tissues that contain edema and blood. *Black line* demarcates the brain bound found from skull stripping . . . . . 109

Figure 5.4 Region growing/shrinking. The seeds identified (see Figure 5.3) from the asymmetry undergo diffusion of T2 asymmetric values for region growing/shrinking for either blood or edema. This example is from a TBI animal. The *black bar* on the color bar is the threshold. . . . . 112

Figure 5.5 Comparison of lesion visualization. Temporal (1, 3 and 14 days post injury) of repetitive TBI and sham animals where compared to naive animals in which no lesion was identified. Both T2 maps and T2-weighted image (T2WI) illustrate the raw data with the results of our automated algorithm shown in the two *right panels*. As can be seen, the algorithm allows accurate demarcation of evolving blood and edema in brain tissues that were validated against the gold-standard manual lesion detection . . . . . 113

Figure 6.1 Comparison of resolution and imaging depth for functional magnetic resonance imaging (fMRI), ultrasound, OCT, and confocal microscopy . . . . . 120

Figure 6.2 Michelson interferometer with a beam splitter . . . . . 121

Figure 6.3 **a** SD-OCT System Diagram: superluminescent diodes (SLDs), line scan camera (lsc), mirror (m), galvanometers (gm), grating (gr). Image of a mouse skull with raster scanning pattern for volume data acquisition represented by *solid* and *dashed arrows*. **b** dB grayscale OCT image: thinned skull (s), cerebral cortex (ctx), corpus callosum (cc), scale bar: 0.5 mm. **c**  $3D\ 4 \times 2 \times 2$  mm volume rendering of 200 grayscale images. . . . . 123

Figure 6.4 A-line preprocessing schematic. **a** Fringe magnitude with respect to the pixel array for one A-line. **b** Wavelength array  $W'$  with respect to wavenumber used to correct wavenumber assignment in each pixel in (a). IP: Interpolation step of A with respect to B. **c** Resulting dB intensity A-line with depth (mirror image removed). **d** Resulting fringe magnitude plot post-IP with correct wavenumber assignment. FFT: Fast Fourier Transform. . . . . 124

Figure 6.5 Normalized average intensity ( $N$ ) from an ROI plotted over time. The three arrows from *left* to *right* represent saline injection, PTZ injection, and initiation of full seizure, respectively. The shaded region is the 2SD of the 10 min baseline . . . . . 126

Figure 6.6 SD-OCT grayscale intensity volume ( $4 \times 2 \times 2$  mm) of mouse cortical tissue (*left*) and its  $fOCT$  volume (48 min) (*right*). *Color bar* represents ratio values  $\pm 50\%$  away from a  $0\%$  change at baseline. . . . . 128

Figure 6.7 MIP frames of cortical volumes. Numbers are time (min) of volume. 0–32: Control, 4–56: Seizure activity, 64: post-overdose. Color is scaled to the *color bar* in Figure 6.6 and represents ratio values  $\pm 50\%$  away from a  $0\%$  change at baseline. *Scale bar* 1 mm. See Media 1: <https://www.youtube.com/watch?v=3ylu3oHZEC4>. . . . . 129

Figure 6.8 Frames of cortical tissue volumes with functional maps applied. Volumes are  $4 \times 2 \times 2$  mm Numbers are time (min) of volume. 0–32: Control, 40–56: Seizure activity, 64: post-overdose. *Color bar* percent change from baseline ( $0\%$ ) saturating at  $\pm 50\%$ . *Scale bar* 1 mm. See Media 2: <https://www.youtube.com/watch?v=sfNhuK9JSxA>. . . . . 130

Figure 7.1 **a** Unattached single stem cell; **b** substrate-attached single stem cell; **c** dynamically blebbing stem cell; **d** apoptotically blebbing stem cell; **e** apoptotic stem cell . . . . . 136

Figure 7.2	<b>a</b> Image of hESCs taken with 10× objective; <b>b</b> Image of hESCs taken with 20× objective; <b>c</b> Image of hESCs taken with 40× objective . . . . .	137
Figure 7.3	True positive rate versus false positive rate (ROC curves) ( <i>Note the red squares are the optimal results of the proposed method</i> ). . . . .	145
Figure 7.4	A sample of results of unattached single stem cell detection approach . . . . .	146
Figure 7.5	<b>a–c</b> Median filter-induced texture-based method results for 10×, 20×, and 40× images respectively; ( <b>d–f</b> ) entropy-based k-means method results for 10×, 20×, and 40× images, respectively; ( <b>g–i</b> ) gradient magnitude distribution-based method results for 10×, 20×, and 40× images, respectively. . . . .	147
Figure 8.1	Comparison of CL-Quant segmentation protocol and ground truth. hESC were plated in mTeSR medium in a 35 mm dish and incubated in a BioStation IM for 4 h. <b>a</b> Phase contrast images modified with ImageJ to remove text labels and the same images with masks applied using the professional CL-Quant protocol. <b>b</b> Graph showing cell area (spreading) in pixels for CL-Quant derived data and the ground truth. The areas obtained from the two methods were in good agreement . . . . .	156
Figure 8.2	Cell area (spreading) was successfully masked by the professional CL-Quant protocol in different experimental conditions. hESC were treated with ROCK inhibitors (Y27632 and H1152) or blebbistatin, incubated in a BioStation IM for 4 h, and imaged at 1 min intervals. Phase contrast images and the corresponding masked images are shown for hESC treated with: <b>a</b> control medium, <b>b</b> Y27632, <b>c</b> H1152, and <b>d</b> blebbistatin . . . . .	158
Figure 8.3	The morphology and spreading of hESC was affected by treatment with ROCK inhibitors (Y27632 and H1152) and blebbistatin in two experiments. Spreading was measured using the professional CL-Quant protocol. <b>a</b> Phase contrast images from the first experiment showed that treated cells were morphologically different than the control. <b>b</b> The rate of spreading and the fold increase in spread area was greater in Y27632 and blebbistatin treated cells than in controls. <b>c</b> Phase contrast images of control and treated cells in the second experiment showed morphological changes in	

the treated groups. **d** The fold increase in spread area was greater in the treated cells than in the controls in the second experiment; however, the effect of Y27632 was not as great as previously seen. Data in **(b)** and **(d)** are plotted as a percentage of the area in the first frame. Each point is the mean  $\pm$  the SEM. . . . . 159

Figure 8.4 Comparison of the professional and user-generated cell spreading protocols. **a** Phase contrast micrographs of hESC treated with Y27632 and the corresponding masks created with the professional and user-generated protocols. **b** Comparison of ground truth to area (spreading) data obtained with the professional protocol in control and treated groups. **c** Comparison of ground truth to area (spreading) data obtained with the user-generated protocol in control and treated groups . . . . . 160

Figure 8.5 Differences in cell morphology showing why treated hESC are more difficult to segment than control cells. **a** Phase contrast image of hESC colonies taken at 60 min of incubation. Segmentation of the image in “**(a)**” created with the user-generated protocol **(b)** and the professional protocol **(c)**. **d** Phase contrast image of hESC colonies treated with Y27632 for 60 min. The cells have many thin surface projections not present on controls. Segmentation of the image in “**(c)**” with the user-generated protocol **(e)** and the professional protocol **(f)** . . . . . 161

Figure 9.1 Growth of hiPSC colonies over 48 h. **a–c** Phase contrast images of control iPSC colonies at various times during growth. **d–f** The same control images segmented using a CL-Quant protocol developed in our lab. **g–i** Phase contrast images of smoke treated iPSC colonies at various times during growth. **j–l** The same treatment group images masked using the same CL-Quant protocol as applied to control colonies. **m** Graph of control and treated cells showing growth rate. Data are means and standard errors of three experiments. *CN* control . . . . . 172

Figure 9.2 Growth of single mNSC. **a–c** Phase contrast images of control mNSC at various times during growth over 48 h. **d–f** The same images after segmentation using a protocol developed by DR Vision. **g** Graph showing analysis for growth rate of control and treated cells (*solid lines*) and ImageJ ground-truth for each group (*dotted lines*). **h** Graph of control and treated mNSC



showing confluency rate. Data are means and standard errors of three experiments. *CN* control . . . . . 173

Figure 9.3 Migration of hESC colonies. **a** Masked phase contrast image of a growing hESC colony during migration. **b** Masked phase contrast image of a shrinking hESC colony during migration. **c** Masked phase contrast image of a dying hESC colony during migration. **d**, **e** Graphs showing total displacement/distance traveled for each control and treated colonies. All CL-Quant masking and tracking of colonies were done by applying a tracking recipe developed by our lab. *CN* control . . . . . 175

Figure 9.4 Diagram of Ibidi gap closure culture inserts . . . . . 176

Figure 9.5 Gap closure for mNSC and NTERA2 cells. **a–c** Phase contrast images of mNSC at various 3 times during gap closure. **d–f** The same images after segmentation using a protocol developed in our lab with CL-Quant software. **g**, **h** Graph showing rate of gap closure for control (*blue*) and treated NTERA2 cells (*red*) and the corresponding ground-truth (*dotted lines*) obtained using ImageJ. **i** Graph of mNSC migration by monitoring percent of gap closure over 44 h. **j** Graph of NTERA2 cell migration by monitoring percent of gap closure over 44 h. Data are means and standard errors of three experiments. . . . . 177

Figure 9.6 Production of reactive oxygen species in hPF. **a–d** Merged phase contrast and fluorescent images at various times during incubation of control and treated hPF with MitoSox Red. **e** Graph showing fluorescence intensity in control and treated cells over time. *CN* control . . . . . 179

Figure 9.7 Quantification of neurons in neural differentiation assay. **a–c** Phase contrast images of mNSC at various times during incubation. **d–f** CL-Quant software masking of mNSC phase contrast images to identify the neurons within each frame. **g** Graph showing quantification results obtained using the CL-Quant software was similar to the ground-truth obtained using the ImageJ software . . . . . 181

Figure 10.1 Pattern recognition of membrane compartments in leaf epidermal tissue at cellular and subcellular resolution. Merged confocal laser microscopic images show Arabidopsis leaf epidermal cells. *Top section* GFP-2xFYVE plants were imaged at 403 magnifica-

tion (scale bar = 20 mm) and images analyzed by the endomembrane script. *Bottom section* GFP-PEN1 plants were imaged at 203 magnification (scale bar = 50 mm) and images analyzed by the plasma membrane microdomain script. **a** and **b**, Merged pseudo images. **c** and **d**, Recognition of epidermal cells is shown by *colored lines*. **e**, Recognition of GFP-2xFYVE-labeled endosomal compartments is shown by *colored circles*. **f**, Recognition of **(b)**. Graminis induced GFP-PEN1 accumulation beneath attempted fungal entry sites (indicated by *arrowheads*) is shown by *colored circles*. Color coding is random, different colors indicate individual cells compartments [25]. . . . . 196

Figure 10.2 Cell wall stained by Propidium iodide: **a** Raw data of a test image. **b** After anisotropic diffusion. **c** Watershed segmentation (from local minima) shown in random color. **d** Final segmentation result. **e** Classification of the segments. **f** Manually generated ground-truth for segmentation and classification (modified from Liu et al. [32]) . . . . . 197

Figure 10.3 Representation obtained by automatic tracking method of the same tracking result from a cell tagged with GFP-Rab6. **a** 3D trajectories of the detected objects. The colour indicates the time window when an object was detected. The z projection of the first 3D image of the time-series is shown below the trajectories to visualize the cell morphology (modified from Racine et al. [35]) . . . . . 197

Figure 11.1 Separation of the growth process into key blocks. Cell growth requires the deposition of new cell wall material. This deposition is controlled by internal cellular dynamics, which are by far the most complex part of the process . . . . . 203

Figure 11.2 The dynamics of ROP1 in both the active form (-GTP) and the inactive form (-GDP). In positive feedback (*left-to-right*), ROP1-GTP promotes RIC4, which promotes the assembly of the F-Actin network that conveys ROPGEF to the sites of ROP1-GTP. ROP-GEF converts ROP1-GDP to ROP1-GTP. In negative feedback (*right-to-left*), ROP1-GTP promotes RIC3, which promotes Ca<sup>2+</sup> accumulation. Ca<sup>2+</sup> destroys the F-Actin network and stops the transportation of

ROPGEF. With diminished localized concentration of ROPGEF, global conversion of ROP1-GTP into ROP1-GDP prevails . . . . . 205

Figure 11.3 Representation of ROP1-GTP activity as a 2-state Markov process. The transition from accumulation-to-decay is assumed to be the signal for the start of exocytosis, which leads to growth . . . . . 206

Figure 11.4 Images showing the results of tip tracking for two experimental videos (*rows*) of growing pollen tubes. The number of images in each *row* denotes the number of detected growth cycles. Each image shows the initial tip shape (*yellow*), the models estimate of the final tip shape (*green*) and the observed tip shape (*red*). The first experiment shows straight growth while the second shows both straight and turning tip behavior. Please see Supplemental Materials for a video. . . . . 210

Figure 11.5 ROC plot of average accuracy of predicted shape as pixel acceptance threshold increases from 0 to 10 pixels (0–0.58  $\mu\text{m}$ ). *Error bars* indicate standard deviation. Statistics are obtained for approximately 64 predicted shapes from experiment 1 in Fig. 11.4. Over 90 % accuracy is achieved within 0.1  $\mu\text{m}$  (5.43 % of cell radius) . . . . . 211

Figure 11.6 Elongation trend in the pollen tube shown in Figure 11.4, row 1. The *blue curve* is the cumulative sum of the measured affine parameter for elongation (**b**) and the *red curve (dotted)* shows the fit of Eq. (11.6) to the data for each growth cycle (between *vertical bars*). *Curve agreement* indicates that the Gompertz function is suitable for explaining observed cell wall dynamics . . . . . 211

Figure 12.1 The general workflow in the image analysis pipeline . . . . . 217

Figure 12.2 Registration methodology in sparse confocal image stacks—**a** SAM located at the tip Arabidopsis shoot, **b** raw images taken at consecutive time instances, **c** segmented images after applying watershed segmentation, **d** estimation of the corresponding landmark point pairs, and **e** bottom image is registered to the top image (the *same color arrows* represent the same cell) . . . . . 219

Figure 12.3 **a, d** The local graphs  $G_1$  and  $G_2$  at time  $t$  and  $t + 1$  with the central cells  $C$  and  $C'$ , respectively, and clockwise ordered neighboring cell vertices  $N_1, \dots, N_6$  and  $N'_1, \dots, N'_6$ , **b, c** two enlarged triangle subgraphs with

indicated features  $N_{i_1}, N_{i_2}$ — $i_1$ th and  $i_2$ th neighboring cells of  $C$ ,  $N'_{j_1}, N'_{j_2}$ — $j_1$ th and  $j_2$ th neighboring cells of  $C'$ ,  $\theta_{N_{i_1}, C, N_{i_2}}(t)$ —angle between  $\overline{N_{i_1}C}$  and  $\overline{N_{i_2}C}$ ,  $\theta_{N'_{j_1}, C', N'_{j_2}}(t)$ —angle between  $\overline{N'_{j_1}C'}$  and  $\overline{N'_{j_2}C'}$ ,  $l_{C, N_{i_1}}(t)$ ,  $l_{C, N_{i_2}}(t)$ —neighbor edge lengths,  $l_{C', N'_{j_1}}(t+1)$ ,  $l_{C', N'_{j_2}}(t+1)$ —edge lengths,  $A_{N_{i_1}}(t), A_{N_{i_2}}(t)$ —areas of the cells  $N_{i_1}, N_{i_2}$ ,  $A_{N'_{j_1}}(t+1), A_{N'_{j_2}}(t+1)$ —areas of the cells  $N'_{j_1}, N'_{j_2}$  . . . . . 220

Figure 12.4 **a** Raw consecutive images (the *same color arrows* represent the same cells) and tracking results obtained **b** without registration **c** with MIRIT registration, **d** with manual registration, and **e** with proposed automatic registration. The *same colors* represent the same cell. **f** Number of tracked cells across two consecutive images. **g** Length of cell lineages . . . . . 222

Figure 12.5 The overall diagram of the adaptive cell segmentation and tracking scheme. . . . . 223

Figure 12.6 Optimization Scheme. **a** Schematic showing how to integrate the spatial and temporal trackers for 4D image stacks. **b** Adaptive segmentation and tracking scheme for a certain image slices  $S'_k$  (the  $k$ th slice at the  $t$  time point) . . . . . 225

Figure 12.7 The segmentation and tracking results using adaptive method. . . . . 227

Figure 12.8 The segmentation and tracking results in 3D stacks at selected time instances. The segmented cells shown in *same color* across consecutive slices (second, third, and fourth slices) represent same cells . . . . . 227

Figure 12.9 Visualization of the AQVT-based 3D reconstruction of SAM cell cluster. **a** Visualization of the 3D reconstructed structure of a cluster of around 220 closely packed cells using convex polyhedron approximations of the densely clustered data points for each cell, as obtained from the proposed 3D reconstruction scheme, **b** a subset of cells from the same tissue . . . . . 232

Figure 12.10 Reconstruction of a cluster of cells using Euclidean distance-based Voronoi tessellation and the proposed AQVT for comparison of the 3D reconstruction accuracy. **a** Segmented and tracked cell slices for a cluster of 52 cells from the L1 and L2 layers of SAM. A dense confocal image stack is subsampled at a  $z$ -resolution of 1.35  $\mu\text{m}$  to mimic the ‘ $z$ -sparsity’

observed in a typical Live-Imaging scenario. The slices belonging to the same cell are marked with the same number to show the tracking results. **b** 3D reconstructed structure for a subset of these cells when reconstructed using the Euclidean distance-based Voronoi Tessellation. **c** The AQVT-based reconstruction result for the same cell cluster. . . . . 233

Figure 13.1 *N. crassa* life cycle. *Neurospora* grows by extension, branching, and fusion of hyphae to form a colony. *Neurospora* has two asexual sporulation pathways (macroconidiation and microconidiation) and a sexual cycle . . . . . 239

Figure 13.2 Automated analysis of hyphal cell compartments. (Left) Image of hyphae stained with Calcofluor-white. (Right) Demonstration of automatic analysis software results before selection of *Neurospora* regions. . . . . 242

Figure 13.3 Determination of hyphal growth rate. **a** Length of the midline of the hypha over time. The *green dashed line* is the smoothed measurements from the *solid blue line*. The smoothed measurements were obtained with a moving average. **b** Rate of change in length of the hypha over time (velocity). The results show that hyphal growth is oscillating over time . . . . . 244

Figure 13.4 Conidia images. Original image (left) and after being subjected to Gabor filtering (right). . . . . 245

Figure 13.5 Halo intensity histogram. The halo intensity distribution is located at the *right* of the histogram, while the background distribution is on the *left*. As the result, the halo stands out as part of detected cell regions by Otsu's . . . . . 246

Figure 14.1 Multifactorial experimental design and associated images can be visualized through the web. Each row corresponds to thumbnail views of samples prepared and imaged with the same set of experimental factors . . . . . 254

Figure 14.2 **a** An example of  $\gamma$ H2AX and 53BP1 co-localization on a cell-by-cell basis. *Blue* is the DAPI (nuclear) stained channel. *Green* corresponds to  $\gamma$ H2AX, and red corresponds to 53BP1. **b** Each nucleus and the corresponding sites of foci are segmented . . . . . 255

Figure 14.3 Steps in delineating clumps of nuclei . . . . . 257

Figure 14.4 Detection of foci on a cell-by-cell basis for two nuclei . . . . . 258

Figure 14.5 Representative phenotypic signatures of the DNA repair sites, as a function of time, indicates that the repair mechanism is typically complete within the first 15 h following the radiation exposure. . . . . 260

Figure 14.6 **a** Amount of colocalization of 53BP1 (source channel) and  $\gamma$ H2AX (target channel) foci in 2D cultures of stationary MCF10A cells after iron ion exposure over time. The amount of foci overlap is given in parenthesis. Data points represent the average of three independent experiments. **b** Amount of colocalization of 53BP1 (search channel) and  $\gamma$ H2AX (target channel) foci in 2D cultures of cycling MCF10A cells after iron ion exposure over time. Amount of foci overlap is given in parenthesis. Data points represent the average of two independent experiments. **c** Amount of co-localization of 53BP1 (source channel) and  $\gamma$ -H2AX (target channel) foci in 2D cultures of stationary MCF10A cells after iron ion exposure over time for 50 % (0.5) foci overlap. Error bars represent the standard deviation of three independent experiments. . . . . 261

Figure 15.1 Cofilin Modulation in Dendritic Spines. The activity of cofilin can be regulated by altering its phosphorylation state: (1) NMDAR-mediated  $Ca^{2+}$  influx, which activates calcineurin and dephosphorylates cofilin by SSH; (2) Rac1-PAK1-LIMK signaling cascade downstream of Ephrin/EphB receptors, which phosphorylates cofilin; and (3) activation via a light-controllable PA-Rac1. Pathway (1, green) can lead to F-actin severing and loss and/or reorganization of dendritic spines, or formation of cofilin-actin aggregates called rods. Pathways (2, red) and (3) are proposed to lead to polymerization of F-actin and stabilization of spines. . . . . 267

Figure 15.2 Experimental schematics of cell culture, transfection, and photoactivation methods of the hippocampal neurons. **a** Primary hippocampal neurons were isolated from the hippocampus of embryonic day 15–16 (E15-16) mice, dissociated enzymatically, plated onto poly-D-lysine and laminin-plated glass coverslips, and allowed to mature in culture for 1–4 weeks. **b** The cultures were transfected at 14 days in vitro (DIV) using calcium phosphate method to overexpress PA-Rac and GFP-tagged-wt-Cofilin (shown in green). The live changes in cofilin localization were recorded by tracking the GFP signal, while simultaneously